3

Electronic Properties of Interfaces and Defects from Many-body Perturbation Theory: Recent Developments and Applications

Matteo Giantomassi, Martin Stankovski, Riad Shaltaf, Myrta Grüning, Fabien Bruneval, Patrick Rinke, and Gian-Marco Rignanese

3.1
Introduction

Almost all electronic and optoelectronic devices (such as MOS transistors, photovoltaic cells, semiconductor lasers, etc.) contain metal–semiconductor, insulator–semiconductor, insulator–metal, and/or semiconductor–semiconductor interfaces. The electronic properties of such heterojunctions determine the device characteristics [1, 2]. The band gaps of the participating materials are usually different, hence, at least one of the band edges is different. The energy of charge carriers must then change when passing through the heterojunction. Most often, there will be discontinuities in both the conduction and valence bands. These so-called band offsets (BOs) are the origin of most of the useful properties of heterojunctions.

Defects also play a critical role for the functionality of devices [3–5]. They can have both positive as well as detrimental effects. As dopants they provide charge carriers in semiconductors, which can contribute to a current, but these carriers can also recombine at defect sites and are then lost. Problems like flat-band and threshold voltage shifts, carrier mobility degradation, charge trapping, gate dielectric wear-out, and breakdown, as well as temperature instabilities are believed to mainly originate from defects forming at (or close to) the heterojunction interface. A deep understanding of the defects concerned is thus highly desirable for the enhancement of device performance.

However, experimental characterization of defect energy levels at interfaces is often very difficult to achieve, so theoretical simulation can provide extremely useful information for further improvement of devices. In this framework, density functional theory (DFT) has been, and still is, widely used to investigate the electronic properties of various defective interfaces. Unfortunately, the semi-local approximations to DFT – such as the local density approximation (LDA) or the generalized-gradient approximation (GGA) – suffer from a well-known

substantial underestimation of band gaps, which hinders a precise prediction of the energy-level alignment at interfaces. For this reason, hybrid density functionals have recently increased in popularity [6–11]. These functionals, which incorporate a fraction of Hartree-Fock (HF) exchange, lead to higher accuracies [12] and improved band gaps [13, 14] compared to corresponding results using semilocal functionals. The fraction of HF exchange to be included cannot be known in advance for all materials and its optimal value could even be property dependent [15, 16]. Therefore the reliability of hybrid density functionals cannot be assessed *a priori* [17].

In contrast, many-body perturbation theory (MBPT) [18–22] offers an approach for obtaining quasiparticle (QP) energies in solids which is controlled and amenable to systematic improvement. However, the cost of such calculations is generally higher than that of their DFT counterparts. Recently, considerable effort has been devoted to finding reliable techniques to speed up MBPT calculations and make them tractable for the larger systems needed to simulate defects and interfaces.

In this chapter, we will review the recent developments in MBPT calculations and the results obtained for interfaces and defects. Section 3.2 is devoted to the theoretical basis of MBPT. Hedin's equations are presented in Section 3.2.1. The GW approximation is introduced in Section 3.2.2, while approximations going beyond GW are discussed in Section 3.2.3. Section 3.3 focuses on the practical implementation and the recent developments of MBPT. In Section 3.3.1, we describe the perturbative approach, that is usually employed to obtain QP energies. The methods used to take into account the frequency dependence of the self-energy operators are presented in Section 3.3.2. In order to allow for a reduction of the number of unoccupied states that need to be included explicitly in the calculations, the extrapolar method is introduced in Section 3.3.3. We discuss the combination of MBPT with the projector-augmented wave (PAW) method in Section 3.3.4. Sections 3.4 and 3.5 are dedicated to MBPT results obtained for BOs at interfaces and for defects, respectively. Special emphasis is put on the caveats of the methods.

3.2
Many-Body Perturbation Theory

3.2.1
Hedin's Equations

A rigorous formulation for the properties of QPs is based on a Green's function approach [18]. The QP energies E_i^{QP} and wavefunctions ψ_i^{QP} are obtained by solving the QP equation:

$$\left\{ -\frac{1}{2}\nabla^2 + V_{\text{ext}}(\boldsymbol{r}) + V_{\text{H}}(\boldsymbol{r}) \right\}\psi_i^{QP}(\boldsymbol{r}) + \int \Sigma(\boldsymbol{r}, \boldsymbol{r}'; E_i^{QP})\psi_i^{QP}(\boldsymbol{r}')d\boldsymbol{r}' = E_i^{QP}\psi_i^{QP}(\boldsymbol{r}),$$

$$(3.1)$$

where V_{ext} and V_H are the external and Hartree potentials, respectively. In this equation, the exchange and correlation effects are described by the electron self-energy operator $\Sigma(r, r', E_i^{QP})$ which is non-local, energy dependent, and non-Hermitian. Hence, the eigenvalues E_i^{QP} are generally complex: their real part is the energy of the QP, while their imaginary part gives its lifetime.

The main difficulty is to find an adequate approximation for the self-energy operator Σ. Hedin [23] proposed a perturbation series expansion in the fully screened (as opposed to bare) Coulomb interaction. The Green's function, G_0, of a "zeroth-order" system of non-interacting electrons is first constructed from the one-particle wavefunctions ψ_i and energies E_i of the "zeroth-order" Hamiltonian, as:

$$G_0(r, r', E) = \sum_i \frac{\psi_i(r)\psi_i^*(r')}{E - E_i + i\eta \mathrm{sgn}(E_i - \mu)}, \tag{3.2}$$

where μ is the chemical potential and η is a positive infinitesimal. The exact one-body Green's function G is thus written using the Dyson equation:[1]

$$G(12) = G_0(12) + \int G_0(13)\Sigma(34)G(42)d(34). \tag{3.3}$$

Here, the self-energy Σ is obtained by self-consistently solving Hedin's closed set of coupled integro-differential equations:

$$\Gamma(12; 3) = \delta(12)\delta(13)$$
$$+ \int \frac{\delta\Sigma(12)}{\delta G(45)} G(46)G(75)\Gamma(67; 3)d(4567), \tag{3.4}$$

$$P(12) = -i \int G(23)G(42^+)\Gamma(34; 1)d(34), \tag{3.5}$$

$$W(12) = v(12) + \int W(13)P(34)v(42)d(34), \tag{3.6}$$

$$\Sigma(12) = i \int G(14)W(1^+3)\Gamma(42; 3)d(34), \tag{3.7}$$

where P is the polarizability, W the screened and v the unscreened Coulomb interaction and Γ the *vertex* function, which describes higher-order corrections to

---

1) In Section 3.1, Hedin's simplified notation $1 \equiv (x_1, \sigma_1, t_1)$ is used to denote space, spin, and time variables and the integral sign stands for summation or integration of all of these where appropriate. 1^+ denotes $t_1 + \eta$ where η is a positive infinitesimal in the time argument. Atomic units are used in all equations throughout this paper.
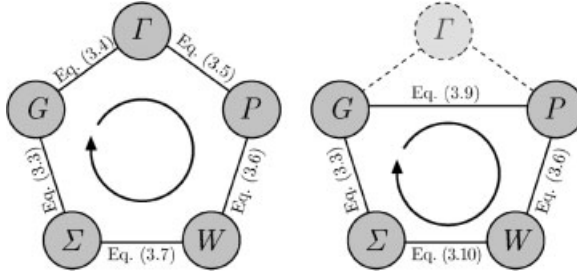
Figure 3.1 Graphical illustration of the self-consistent process required to solve the complete set of Hedin's equations (left panel) and the four coupled integro-differential equations resulting from the GW approximation (right panel). The so-called $G_0 W_0$ approximation consists of performing the loop only once starting from $G = G_0$.

the interaction between quasiholes and quasielectrons. The self-consistent iterative process is illustrated in the left panel of Figure 3.1.

The most complicated term in these equations is Γ, which contains a functional derivative and hence cannot in general be evaluated numerically. The vertex is the usual target of simplification for an approximate scheme.

3.2.2
GW Approximation

Hedin's GW method [23] is the most widely used approximation for the self-energy, Σ. The approximation is defined by neglecting the variation of the self-energy with respect to the Green's function $\delta\Sigma(12)/\delta G(45) = 0$ in Eq. (3.4), leading to:

$$\Gamma(12;3) = \delta(12)\delta(13). \tag{3.8}$$

Thus, the polarizability in Eq. (3.5) is given by:

$$P(12) = -iG(12^+)G(21), \tag{3.9}$$

which corresponds to the random phase approximation (RPA) for the dielectric matrix. The self-energy in Eq. (3.7) becomes simply a product of the Green's function and the screened Coulomb interaction:

$$\Sigma(12) = iG(12)W(1^+2), \tag{3.10}$$

where the Green's function used is consistent with that returned by Dyson's equation.

Since the self-energy depends on G, this procedure should be carried out iteratively, beginning with $G = G_0$, until the input Green's function equals the output one. This yields the self-consistent GW approximation, in which the self-consistent cycle is restricted to Eqs. (3.3), (3.9), (3.6), and (3.10), as illustrated in the right panel of Figure 3.1.

In practice, it is customary to use the first iteration only, often called one-shot GW or G_0W_0, to approximate the self-energy operator. Here, W_0 is perhaps the simplest possible screened interaction, which in terms of Feynman diagrams involves an infinite geometric series over non-interacting electron–hole pair excitations as in the usual definition of the RPA.[2] This approximation for W, although tremendously successful for weakly correlated solids, is not free of self-screening errors [24, 25].

When using only a single iteration, it is important to make that one as accurate as possible, so an initial G_0 calculated using Kohn–Sham DFT is normally used. The logic is that the Kohn–Sham orbitals should produce an input G_0 much closer to the self-consistent solution, thus rendering a single iteration sufficient. This choice of G_0 has in the past produced accurate results for QP energies (i.e., the correct electron addition and removal energies, in contrast to the DFT eigenvalues [26]) for a wide range of s–p bonded systems [27]. However, because this choice of G_0 corresponds to a non-zero initial approximation for Σ_0, there is no longer a theoretical justification for the usual practice of setting the vertex to a product of delta functions before the decoupling. Also, different choices for the exchange-correlation functional may lead to different Green's functions [28, 29], making G_0W_0 results dependent on the starting point.

3.2.3
Beyond the *GW* Approximation

Since G_0 is often constructed from DFT orbitals, the self-energy and its derivative are not zero for the first iteration. Using the static exchange-correlation kernel, K_{xc}, (which is the functional derivative of the DFT exchange-correlation potential, V_{xc}, with respect to density, n) Del Sole *et al.* [30] demonstrated how G_0W_0 may be modified with a vertex function to make Σ consistent with the DFT starting point. They added the contribution of the vertex – decoupled after the first evaluation of $\delta\Sigma(12)/\delta G(45)$ in Eq. (3.4) – into both the self-energy, Σ (3.7), and the polarization, P (3.5). The result is a self-energy of the form $G_0W_0\Gamma$. Instead, the $G_0\widetilde{W}_0$ approximation is obtained when the vertex function is included in P *only*. As commented by Hybertsen and Louie [31] and Del Sole *et al.*, both these results take the *form* of GW, but with W representing the Coulomb interaction screened by the test-charge-electron dielectric function and the test-charge-test-charge dielectric function, respectively, and with electronic exchange and correlation included through a time-dependent DFT (TDDFT) kernel.

Using the LDA for the exchange-correlation potential and kernel, Del Sole *et al.* found that $G_0W_0\Gamma$ yields final results almost equal to those of G_0W_0 for the band gap of crystalline silicon and that the equivalent results from $G_0\widetilde{W}_0$ were shown to close the gap slightly compared to standard G_0W_0. However, in this previous study the

---

2) In contrast to the common use of the RPA, there is no integration over the interaction strength, since the perturbation expansion itself takes care of the switching on of interactions.

PPM approximation was utilized for modeling the frequency-dependence of W, which may have affected the resulting QP energies.

3.3
Practical Implementation of *GW* and Recent Developments Beyond

3.3.1
Perturbative Approach

Often, it is more efficient to obtain the QP energies from Eq. (3.1) rather than solving the Dyson equation (Eq. 3.3) and searching for the poles of the Green's function. The approach consists of using perturbation theory with respect to the results of DFT. Despite some fundamental differences, the formal similarity is striking between the QP equation and the Kohn–Sham equation:

$$\left\{ -\frac{1}{2}\nabla^2 + V_{\text{ext}}(\boldsymbol{r}) + V_{\text{H}}(\boldsymbol{r}) \right\} \psi_i^{\text{DFT}}(\boldsymbol{r}) + V_{\text{xc}}(\boldsymbol{r})\psi_i^{\text{DFT}}(\boldsymbol{r}) = E_i^{\text{DFT}}\psi_i^{\text{DFT}}(\boldsymbol{r}),$$

(3.11)

where V_{xc} is the DFT exchange-correlation potential.[3] In many cases, the DFT energies E_i^{DFT} already provide a reasonable estimate of the band structure and are usually in qualitative agreement with experiment. Furthermore, in the simple systems for which the true QP amplitudes ψ_i^{QP} have been calculated, it was found that the DFT wave functions ψ_i^{DFT} are usually very close to the QP results [31, 32]. In silicon, for instance, the overlap between DFT-LDA and QP wave functions has been reported to be close to 99.9%, but for certain surface [33, 34] and cluster states [35, 36] the overlap is far less (see also Ref. [37] for comments and criticisms). This indicates that in the basis of Kohn–Sham wave functions, the self-energy can be considered a diagonally dominant matrix with negligible off-diagonal elements.

Hence, E_i^{DFT} and ψ_i^{DFT} for the ith state are used as a zeroth-order approximation for their QP counterparts. The QP energy E_i^{QP} is then calculated by adding to E_i^{DFT} the first-order perturbation correction which comes from replacing the DFT exchange-correlation potential V_{xc} with the self-energy operator Σ:

$$E_i^{\text{QP}} = E_i^{\text{DFT}} + \left\langle \psi_i^{\text{DFT}} | \Sigma(E_i^{\text{QP}}) - V_{\text{xc}} | \psi_i^{\text{DFT}} \right\rangle.$$

(3.12)

To solve Eq. (3.12), the energy dependence of Σ must be known analytically, which is usually not the case. Under the assumption that the difference between QP and DFT energies is relatively small, the matrix elements of the self-energy operator can

---

3) Note that V_{xc} can be seen as a static, local, and hermitian approximation to $\Sigma(12)$.

be Taylor expanded to first-order around E_i^{DFT} in order to be evaluated at E_i^{QP}:

$$\Sigma\left(E_i^{\text{QP}}\right) \approx \Sigma\left(E_i^{\text{DFT}}\right) + \left(E_i^{\text{QP}} - E_i^{\text{DFT}}\right)\frac{\partial\Sigma(E)}{\partial E}\Bigg|_{E=E_i^{\text{DFT}}}. \qquad (3.13)$$

In this expression, the QP energy, E_i^{QP}, can be solved for:

$$E_i^{\text{QP}} = E_i^{\text{DFT}} + Z_i\left\langle\psi_i^{\text{DFT}}|\Sigma(E_i^{\text{DFT}}) - V_{\text{xc}}|\psi_i^{\text{DFT}}\right\rangle, \qquad (3.14)$$

where Z_i is the *renormalization factor* defined by:

$$Z_i^{-1} = 1 - \left\langle\psi_i^{\text{DFT}}|\frac{\partial\Sigma(E)}{\partial E}\Bigg|_{E=E_i^{\text{DFT}}}|\psi_i^{\text{DFT}}\right\rangle. \qquad (3.15)$$
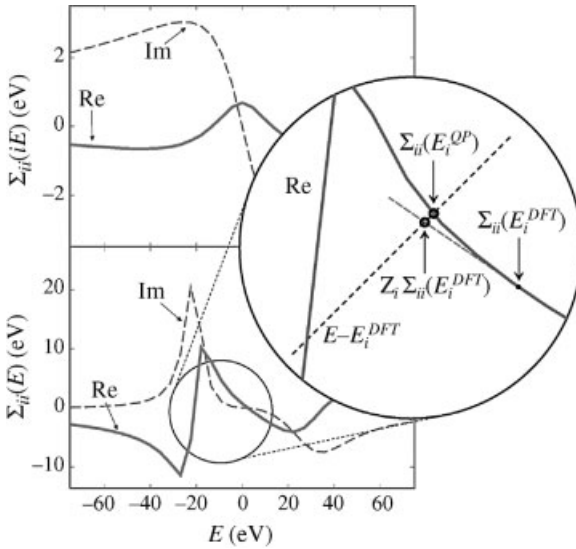
The principle is illustrated in Figure 3.2.

Figure 3.2 (online color at: www.pss-b.com) Schematic illustration (adapted from Ref. [38]) of the perturbative approach to finding the QP correction. In principle, the self-energy matrix element, $\Sigma_{ii}(E) = \langle\psi_i^{\text{DFT}}|\Sigma(E) - V_{\text{xc}}|\psi_i^{\text{DFT}}\rangle$, and the true QP correction, $\Sigma(E_i^{\text{QP}})$, is found from the solution of $E - E_i^{\text{DFT}} = \Sigma_{ii}(E)$, i.e., at the crossing of the dashed black line and $\Sigma_{ii}(E)$ in the circular zoom-in. In practice, the perturbative approach exploits the fact that it is more computationally feasible to use the Taylor expansion around $\Sigma(E_i^{\text{DFT}})$ [Eqs. (3.14) and (3.15)], and find an approximate value for the QP correction at the crossing of the red and black dashed lines.

3.3.2
QP Self-Consistent *GW*

The procedure described above has proven very efficient [27], but several questions inevitably arise: How much does the $G_0 W_0$ result depend on the starting point? What happens if the starting DFT band structure is qualitatively wrong[4]? A self-consistent *GW* self-energy calculation should be free of such concerns.

However, performing self-consistency in *GW* is everything but straightforward, since Σ, being non-Hermitian and energy-dependent, should have non-orthogonal and energy-dependent left and right eigenvectors. In practice, for large systems, the solution of this Hamiltonian is not tractable without approximations. Furthermore, fully self-consistent *GW* calculations have been shown to worsen results compared to the standard one-shot $G_0 W_0$ method [39–41].

A different solution to the self-consistency issue is the so-called QP self-consistent *GW* approximation (QS*GW*) developed by Faleev *et al.* [42] and co-workers [43, 44]. For a set of trial QP energies and amplitudes $\{E_i, \psi_i\}$ (for instance, the eigensolutions of the DFT or Hartree problem), the one-particle Green's function, G, and in turn the *GW* self-energy can be calculated. These authors proposed to constrain the dynamical *GW* self-energy to be static and Hermitian and as close as possible to the one-shot self-energy ($G_0 W_0$) of a non-interacting reference system. Their model QS*GW* self-energy $\widetilde{\Sigma}$ reads:

$$\left\langle \psi_i | \widetilde{\Sigma} | \psi_j \right\rangle = \frac{1}{2} \mathcal{H}[\langle \psi_i | \Sigma(E_i) | \psi_j \rangle + \langle \psi_j | \Sigma(E_j) | \psi_i \rangle], \tag{3.16}$$

where $\mathcal{H}$ means that only the Hermitian part of the matrix is considered.

The approximated self-energy matrix, $\widetilde{\Sigma}$, is diagonalized yielding a new set of orthogonal QP amplitudes and real-valued QP energies. From this new set of orbitals, a new density $n(\mathbf{r})$ and the corresponding Hartree potential is generated, a new $\widetilde{\Sigma}$ is constructed and the procedure is iterated to self-consistency. Ideally, the final result should not depend on the initial Hamiltonian, though no firm mathematical proof for this has been reported so far. The QS*GW* approach improves the $G_0 W_0$ results, giving band gaps very close to experiments with errors that are small and highly systematic [43].

Following the same spirit, Bruneval *et al.* [37] proposed using an alternative Hermitian and static approximation to the *GW* self-energy: the COHSEX approximation, derived by Hedin in 1965 [23]. COHSEX is a simple approximation which consists of two terms, the COulomb Hole part and the Screened EXchange part:

$$\Sigma_{\mathrm{COHSEX}}(\mathbf{r}, \mathbf{r}') = \Sigma_{\mathrm{COH}}(\mathbf{r}, \mathbf{r}') + \Sigma_{\mathrm{SEX}}(\mathbf{r}, \mathbf{r}')$$

$$\Sigma_{\mathrm{COH}}(\mathbf{r}, \mathbf{r}') = \delta(\mathbf{r}, \mathbf{r}')[W(\mathbf{r}, \mathbf{r}', \omega = 0) - v(\mathbf{r} - \mathbf{r}')] \tag{3.17}$$

$$\Sigma_{\mathrm{SEX}}(\mathbf{r}, \mathbf{r}') = -\sum_v \psi_v(\mathbf{r}) \psi_v^*(\mathbf{r}') W(\mathbf{r}, \mathbf{r}', \omega = 0).$$

---

4) For example, if DFT erroneously predicts a system to be metallic, when it is not.

These terms do not involve any summation over empty states (v runs only over occupied states). Performing self-consistency for the COHSEX approximation is hence more tractable than for the QSGW self-energy of Faleev and coworkers, although Σ_{COHSEX} may be a cruder approximation than $\widetilde{\Sigma}$.

An alternative is to constrain the QP amplitudes in $\widetilde{\Sigma}$ to their DFT counterparts and only update the QP energies until convergence. This method is referred to as the eigenvalue-only QSGW (e-QSGW).

3.3.3
Plasmon Pole Models *Versus* Direct Calculation of the Frequency Integral

In the frequency domain, the GW self-energy is given by the convolution

$$\Sigma(\mathbf{r}, \mathbf{r}', \omega) = \frac{i}{2\pi} \int e^{i\omega'\eta} G(\mathbf{r}, \mathbf{r}', \omega + \omega') W(\mathbf{r}, \mathbf{r}', \omega') d\omega', \tag{3.18}$$

where η is a positive infinitesimal. Evaluating this expression requires, in principle, the knowledge of the full frequency dependence of $W(\mathbf{r}, \mathbf{r}', \omega')$. Moreover a fine frequency grid would be required, since $G(\mathbf{r}, \mathbf{r}', \omega)$ and $W(\mathbf{r}, \mathbf{r}', \omega)$ exhibit a fairly complex and rapidly changing frequency dependence on the real axis. There are, however, two different and more efficient techniques to evaluate Eq. (3.18): (i) integration with a PPM and (ii) integration through contour deformation (CD). In the former case, the frequency dependence of $\varepsilon^{-1}(\omega)$ is modeled with a simple analytic form, and the frequency convolution is carried out analytically.

In the latter approach, the integral is evaluated numerically by extending the functions into the complex plane, where the integrand is smoother. Since the fine details of $W(\mathbf{r}, \mathbf{r}', \omega)$ are integrated over in Eq. (3.18), it is reasonable to expect that approximated models, able to capture the main physical features of $W(\mathbf{r}, \mathbf{r}', \omega)$, should give sufficiently accurate results at considerably reduced computational effort. This is the basic idea behind the PPM, in which the frequency dependence of $W(\mathbf{r}, \mathbf{r}', \omega')$ is modeled in terms of analytic expressions. The coefficients of the model are derived from first principles, i.e., without any adjustable external parameters, either by enforcing exact relations or by anchoring the scheme on quantities that are calculated *ab initio*.

It is more convenient to Fourier transform all quantities to a frequency and wave-vector basis using the following convention:

$$W(\mathbf{r}, \mathbf{r}', \omega) = \sum_{\mathbf{q}\mathbf{G}\mathbf{G}'} e^{i(\mathbf{q}+\mathbf{G})\cdot\mathbf{r}} W_{\mathbf{G}\mathbf{G}'}(\mathbf{q}, \omega) e^{-i(\mathbf{q}+\mathbf{G}')\cdot\mathbf{r}'}, \tag{3.19}$$

where $\mathbf{G}$ is a reciprocal lattice vector and $\mathbf{q}$ is a vector in the first Brillouin zone. The screened interaction is related to the dielectric matrix by:

$$W_{\mathbf{G}\mathbf{G}'}(\mathbf{q}, \omega) = \varepsilon^{-1}_{\mathbf{G}\mathbf{G}'}(\mathbf{q}, \omega) v(\mathbf{q} + \mathbf{G}'), \tag{3.20}$$

where the Fourier transform of the bare Coulomb interaction takes the usual form $v(\boldsymbol{q}) = 4\pi/(V|\boldsymbol{q}|^2)$, V being the crystal volume. Adopting this formalism, the components with $\boldsymbol{G} \neq \boldsymbol{G}'$ generate the local fields.

Finally, when the vertex is neglected as in Eq. (3.8), the dielectric matrix is related to the polarizability, P, by:

$$\varepsilon_{\boldsymbol{GG}'}(\boldsymbol{q},\omega) = \delta_{\boldsymbol{GG}'} - v(\boldsymbol{q} + \boldsymbol{G})\, \boldsymbol{P}_{\boldsymbol{GG}'}(\boldsymbol{q},\omega), \tag{3.21}$$

which is nothing but the usual RPA when Eq. (3.9) is used to compute P.

In the PPMs of Godby and Needs [45] (GN) and Hybertsen and Louie [31] (HL), the imaginary part of $\varepsilon_{\boldsymbol{GG}'}^{-1}(\boldsymbol{q},\omega)$ is approximated in terms of a delta function centered at the plasmon frequency $\tilde{\omega}_{\boldsymbol{GG}'}(\boldsymbol{q})$ with amplitude $A_{\boldsymbol{GG}'}(\boldsymbol{q})$, i.e.:

$$\Im[\varepsilon_{\boldsymbol{GG}'}^{-1}(\boldsymbol{q},\omega)] = A_{\boldsymbol{GG}'}(\boldsymbol{q}) \times [\delta(\omega - \tilde{\omega}_{\boldsymbol{GG}'}(\boldsymbol{q})) - \delta(\omega + \tilde{\omega}_{\boldsymbol{GG}'}(\boldsymbol{q}))]. \tag{3.22}$$

The real part can then obtained by means of a Kramers–Kronig relation, and becomes:

$$\Re[\varepsilon_{\boldsymbol{GG}'}^{-1}(\boldsymbol{q},\omega)] = \delta_{\boldsymbol{GG}'} + \frac{\Omega_{\boldsymbol{GG}'}^2(\boldsymbol{q})}{\omega^2 - \tilde{\omega}_{\boldsymbol{GG}'}{}^2(\boldsymbol{q})}. \tag{3.23}$$

where $\Omega_{\boldsymbol{GG}'}^2(\boldsymbol{q}) = -A_{\boldsymbol{GG}'}(\boldsymbol{q})\, \tilde{\omega}_{\boldsymbol{GG}'}^2(\boldsymbol{q})$.

The approximation given by Eq. (3.22) is quite reasonable, since experiments and first-principles analysis reveals that $\Im[\Omega_{\boldsymbol{G},\boldsymbol{G}'}(\boldsymbol{q},\omega)]$ is generally characterized by a sharp peak in correspondence to a plasmon excitation at the plasmon frequency, at least for low momentum transfers, $\boldsymbol{q}$.

At this point, one defines a set of physical constraints to determine the parameters entering Eqs. (3.22) and (3.23). The GN and HL PPMs differ in the choice of the particular physical properties or exact relations they aim to reproduce.

In the GN approach, the parameters of the model are derived so that $\varepsilon_{\boldsymbol{GG}'}(\boldsymbol{q},\omega)$ is correctly reproduced at two different frequencies: the static limit ($\omega = 0$) and an additional imaginary point located at the Sommerfeld plasma frequency $i\omega_p$, where $\omega_p = \sqrt{4\pi\varrho}$ with ϱ the number of electrons per volume [46]. After some algebra, the following set of equations defining the plasmon-pole coefficients can be derived:

$$\begin{cases} A_{\boldsymbol{GG}'}(\boldsymbol{q}) = \varepsilon_{\boldsymbol{GG}'}^{-1}(\boldsymbol{q},\omega = 0) - \delta_{\boldsymbol{GG}'} \\[2mm] \tilde{\omega}_{\boldsymbol{GG}'}^2 = \omega_p^2 \left[\dfrac{A_{\boldsymbol{GG}'}(\boldsymbol{q})}{\varepsilon_{\boldsymbol{GG}'}^{-1}(\boldsymbol{q},\omega = 0) - \varepsilon_{\boldsymbol{GG}'}^{-1}(\boldsymbol{q}, i\omega_p)} - 1 \right]. \\[2mm] \Omega_{\boldsymbol{GG}'}^2(\boldsymbol{q}) = -A_{\boldsymbol{GG}'}(\boldsymbol{q})\, \tilde{\omega}_{\boldsymbol{GG}'}^2(\boldsymbol{q}) \end{cases} \tag{3.24}$$

In the HL model, the PPM parameters are calculated so as to reproduce the static limit exactly and to fulfill a generalized *f*-sum rule relating the imaginary part of the

exact $\varepsilon_{GG'}^{-1}(\boldsymbol{q}, \omega)$ to the plasma frequency and the charge density [47, 48]. The final expression for the PPM parameters are:

$$\begin{cases} \Omega_{GG'}^2(\boldsymbol{q}) = \omega_p^2 \, \dfrac{(\boldsymbol{q}+\boldsymbol{G}) \cdot (\boldsymbol{q}+\boldsymbol{G}')}{|\boldsymbol{q}+\boldsymbol{G}|^2} \dfrac{n(\boldsymbol{G}-\boldsymbol{G}')}{n(0)} \\[2ex] \widetilde{\omega}_{GG'}^2(\boldsymbol{q}) = \dfrac{\Omega_{GG'}^2(\boldsymbol{q})}{\delta_{GG'}-\varepsilon_{GG'}^{-1}(\boldsymbol{q}, \omega=0)} \\[2ex] A_{GG'}(\boldsymbol{q}) = -\dfrac{\pi}{2} \dfrac{\Omega_{GG'}(\boldsymbol{q})}{\widetilde{\omega}_{GG'}(\boldsymbol{q})}. \end{cases} \tag{3.25}$$

Models based on Eqs. (3.22) and (3.23) have a number of undesirable features, despite their success. For instance, for some elements with $\boldsymbol{G} \neq \boldsymbol{G}'$, the plasmon poles $\widetilde{\omega}_{GG'}(\boldsymbol{q})$ can become very small or even imaginary which is somewhat unphysical [31].

Two more recent PPM approaches due to Von der Linden and Horsch [49] (vdLH) and Engel and Farid [50] (EF) are expected to be more accurate. The vdLH PPM is derived starting from the spectral decomposition of the symmetrized inverse dielectric matrix:

$$\widetilde{\varepsilon}_{GG'}^{-1}(\boldsymbol{q}, \omega) = \frac{|\boldsymbol{q}+\boldsymbol{G}'|}{|\boldsymbol{q}+\boldsymbol{G}|} \varepsilon_{GG'}^{-1}(\boldsymbol{q}, \omega), \tag{3.26}$$

by assuming that the frequency dependence is solely contained in the eigenvalues (see Ref. [49]). The disadvantage of the vdLH approach is that it satisfies the *f*-sum rule only for the diagonal elements. In the EF PPM, the eigenvalues and the eigenvectors are frequency dependent, and derived from an approximation to the reducible polarizability which is exact both in the static- and high-frequency limit. For further details on this plasmon-pole technique, see Ref. [50].

Since the frequency convolution in Eq. (3.18) can be carried out analytically once the plasmon-pole parameters are known, the PPM technique is an ideal tool for initial convergence studies. It usually proves to be accurate to within 0.1–0.2 eV for states close to the Fermi level, when compared to results obtained with a costly numerical integration of Σ [27]. On the other hand, the accuracy worsens for states far from the gap, especially for low-lying states. To analyze physical properties depending on these, it is necessary to avoid PPM methods, and calculate the frequency dependence of *W* explicitly.

A straightforward numerical evaluation of Eq. (3.18) is problematic due to the fact that *G* and *W* both have poles infinitesimally above and below the real axis. Therefore, a straightforward integration algorithm along the real axis would need evaluations of the integrand precisely in the region where it is ill-behaved. An alternative route to evaluating Eq. (3.18) traces back to the earliest *GW* calculations for the homogeneous electron gas [51]. The Green's function *G* and the screened Coulomb interaction *W* are analytic functions (except along the real axis) and can consequently be analytically continued to the full complex plane. The strategy is to use a deformation of the contour of integration in order to avoid
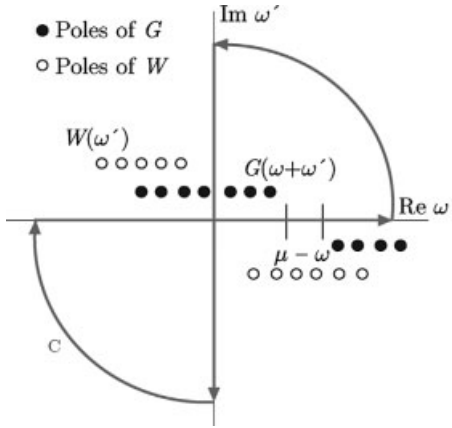
Figure 3.3 (online color at: www.pss-b.com) Schematic representation of the contour of integration in the complex ω' plane used to evaluate $\Sigma(\omega)$. The poles of the integrand are shown as circles. Only the poles due to Green's function that lie inside the path contribute to the final result.

having to deal with quantities close to the real axis as much as possible. Instead of evaluating the integral along the real axis, one evaluates the integral along the imaginary axis, and then adds the residues arising from the poles enclosed in the contour depicted in red in Figure 3.3.

3.3.4
The Extrapolar Method

GW calculations are computationally very demanding. Two major steps in these can be distinguished: the calculation of the polarizability and the evaluation of matrix elements of the self-energy. The quantities involved are not only non-local (two plane-wave indices), but also involve summations over all states (occupied and empty). Recently, Bruneval and Gonze [52] proposed an acceleration scheme to improve the convergence with respect to the number of states. The main idea is to replace the poles arising from the eigenvalues of empty high-energy states with a single (average) pole, which carries all the spectral weight above a certain cutoff for states. Note that the extrapolar technique was first introduced in the optimized effective potential framework [17] and in a preconditioning scheme [53].

Both in the polarizability and in the self-energy, the expressions to be evaluated contain a sum over wavefunctions in a numerator and energy differences in a denominator. If we were able to factor a simple common denominator out of the sum, it would be straightforward to eliminate the wavefunctions in the numerator, above some cutoff band index, N_b, by using the closure relation:

$$\sum_{b > N_b} |b\rangle\langle b| = 1 - \sum_{b \leq N_b} |b\rangle\langle b|. \tag{3.27}$$

Treating the denominator of the remainder (now dependent on all states $b \leq N_b$) is the delicate part, which requires careful consideration.

3.3.4.1 Polarizability with a Limited Number of Empty States

Using time-reversal symmetry, the truncated expression for the independent-particle polarizability in reciprocal and frequency space reads

$$
P_{0\boldsymbol{GG'}}(\boldsymbol{q}, \omega) = \frac{2}{N_{\boldsymbol{k}}\Omega} \sum_{\boldsymbol{k}} \sum_{\substack{N_v < b \leq N_b \\ v \leq N_v}} M_{\boldsymbol{k}}^{bv}(\boldsymbol{q}+\boldsymbol{G})[M_{\boldsymbol{k}}^{bv}(\boldsymbol{q}+\boldsymbol{G'})]^*
$$
$$
\times \left[\frac{1}{\omega-(\varepsilon_{v\boldsymbol{k}}-\varepsilon_{b\boldsymbol{k}-\boldsymbol{q}})-i\eta} - \frac{1}{\omega-(\varepsilon_{b\boldsymbol{k}-\boldsymbol{q}}-\varepsilon_{v\boldsymbol{k}})+i\eta} \right], \tag{3.28}
$$

where Ω is the volume of the unit cell, η is a positive infinitesimal, N_v is the number of valence states, $N_{\boldsymbol{k}}$ is the number of $\boldsymbol{k}$-points in the Brillouin zone, and the index $\boldsymbol{k}$ runs over the $\boldsymbol{k}$-points of the Brillouin zone. The matrix elements:

$$
M_{\boldsymbol{k}}^{bb'}(\boldsymbol{q}+\boldsymbol{G}) = \langle \psi_{b\boldsymbol{k}-\boldsymbol{q}}|e^{-i(\boldsymbol{q}+\boldsymbol{G})\cdot\boldsymbol{r}}|\psi_{b'\boldsymbol{k}}\rangle, \tag{3.29}
$$

are the so-called oscillator strengths.

The extrapolar method proposes that the empty states above the truncation index, N_b, all have the same energy. In this case, the dependence with respect to index b is removed in the denominator and one can apply the closure relation to the numerator in order to get rid of any dependence on this index. This procedure adds a term to the usual truncated expression for P_0. The correction consists of two terms:

$$
\Delta_{\boldsymbol{GG'}}(\boldsymbol{q}, \omega) = \frac{2}{N_{\boldsymbol{k}}\Omega} \sum_{\boldsymbol{k}} \sum_{v \leq N_v} \langle \psi_{v\boldsymbol{k}}|e^{i(\boldsymbol{G'}-\boldsymbol{G})\cdot\boldsymbol{r}}|\psi_{v\boldsymbol{k}}\rangle
$$
$$
\times \left[\frac{1}{\omega-(\varepsilon_{v\boldsymbol{k}}-\overline{\varepsilon}_{P_0})-i\eta} - \frac{1}{\omega-(\overline{\varepsilon}_{P_0}-\varepsilon_{v\boldsymbol{k}})+i\eta} \right]
$$
$$
- \frac{2}{N_{\boldsymbol{k}}\Omega} \sum_{\boldsymbol{k}} \sum_{\substack{b \leq N_b \\ v \leq N_v}} M_{\boldsymbol{k}}^{bv}(\boldsymbol{q}+\boldsymbol{G})[M_{\boldsymbol{k}}^{bv}(\boldsymbol{q}+\boldsymbol{G'})]^*
$$
$$
\times \frac{1}{\omega-(\varepsilon_{v\boldsymbol{k}}-\overline{\varepsilon}_{P_0})-i\eta} - \frac{1}{\omega-(\overline{\varepsilon}_{P_0}-\varepsilon_{v\boldsymbol{k}})+i\eta}, \tag{3.30}
$$

which are now free of any dependence on states above N_b. Instead they contain an "average" energy $\overline{\varepsilon}_{P_0}$ which represents the omitted part of the eigenvalue spectrum by a mean value. The best value for $\overline{\varepsilon}_{P_0}$ can be easily determined by a trial-and-error procedure or in a more elegant manner by considering the fulfillment of the f-sum rule for $P_0(\omega)$.

3.3.4.2 Self-Energy with a Limited Number of Empty States

An analogous procedure can be applied to the correlation part of the self-energy:

$$
\langle \psi_{bk} | \Sigma_c(\varepsilon_{bk}) | \psi_{bk} \rangle = \frac{i}{2\pi N_k \Omega} \int \sum_{b' \leq N_b} \sum_{qGG'} [W_{GG'}(\boldsymbol{q}, \omega') - \delta_{GG'} v(\boldsymbol{q} + \boldsymbol{G})]
$$
$$
\times \frac{M_k^{bb'}(\boldsymbol{q} + \boldsymbol{G})[M_k^{bb'}(\boldsymbol{q} + \boldsymbol{G}')]^*}{\omega' - \varepsilon_{b'k-q} + \varepsilon_{bk} \pm i\eta} d\omega',
$$

(3.31)

where η is a positive infinitesimal. The sign in front of η is plus when the state b' is empty, and minus otherwise.

Unlike for the polarizability, a PPM becomes necessary for the self-energy to make the extrapolar correction tractable. In this context, the PPM is a very good approximation. The final correction reads:

$$
\Delta_{bk} = \frac{1}{N_k \Omega} \sum_{qGG'} \frac{\Omega_{GG'}^2(\boldsymbol{q}) v(\boldsymbol{q} + \boldsymbol{G})}{2\tilde{\omega}_{GG'}(\boldsymbol{q})[\tilde{\omega}_{GG'}(\boldsymbol{q}) + \bar{\varepsilon}_\Sigma - \varepsilon_{bk} - i\eta]}
$$
$$
\times \left\{ \langle \psi_{bk} | e^{i(\boldsymbol{G}' - \boldsymbol{G}) \cdot \boldsymbol{r}} | \psi_{bk} \rangle - \sum_{b' \leq N_b} M_k^{bb'}(\boldsymbol{q} + \boldsymbol{G}) \left[M_k^{bb'}(\boldsymbol{q} + \boldsymbol{G}') \right]^* \right\}.
$$

(3.32)

Again, it consists of two terms that do not depend on any state above N_b. The introduced average energy $\bar{\varepsilon}_\Sigma$ in the denominators can safely be taken to be equal to the previously introduced $\bar{\varepsilon}_{P_0}$.

3.3.5
MBPT in the PAW Framework

Thanks to the excellent agreement obtained with respect to experiments, pseudopotential (PP)-based methods have for several decades represented a *de facto* standard for MBPT calculations. In recent years, however, results obtained with all-electron (AE) approaches [44, 54] have revealed that a fully consistent treatment of the electronic degrees of freedom produces GW band gaps that are systematically smaller than PP results, thus worsening the agreement between G_0W_0 and experiments. These findings have led to quite an intense debate in the scientific literature concerning the reliability of the PP approach for MBPT calculations (see, for instance, Refs. [55–58]).

Systems with shallow cores or localized d- or f-electrons present severe challenges to PP GW calculations [28, 56, 58–60]. Core-valence exchange is large in these systems, due to the large overlap of the localized d or f-states (or semicore states) with lower-lying core states in the same atomic shell. To treat core-valence exchange consistently it is therefore either important to let the exchange part of the GW self-energy act on all electrons of one shell [56, 58, 59] – which can be very expensive computationally – or to build the exchange interaction into the PP [28, 29].

The PAW formalism introduced by Blöchl in 1994 [61] presents a flexible and efficient alternative to PPs in GW calculations. It combines the PP framework with an

AE description and allows for results on a par with AE accuracy at considerably reduced computational cost. The method takes advantage of several ideas and techniques developed in the past decades both in the PP and in the AE community. From the PP approach [62] it inherits the idea of substituting the true Kohn–Sham wave function $\psi(\mathbf{r})$ with a pseudized image $\tilde{\psi}(\mathbf{r})$ which can be efficiently expanded in an extended basis set (e.g., plane-waves). Similar to many AE approaches, PAW employs atomic orbitals to describe the AE wave function $\psi(\mathbf{r})$ inside non-overlapping atom-centered spheres, thus retaining information about the correct nodal structure of electronic orbitals.

The mapping between the true wave function, $|\psi\rangle$, with its complete and complex nodal structure around the nuclei, and the fictitious smooth pseudo wave functions, $|\tilde{\psi}\rangle$, is defined by the linear transformation: $|\psi\rangle = \hat{T}|\tilde{\psi}\rangle$. $\hat{T}$ is given by the identity operator plus a sum of localized terms, $\hat{T}_a$, only acting within the atomic spheres Ω_a centered on atomic sites a:

$$\hat{T} = \hat{1} + \sum_a \hat{T}_a. \tag{3.33}$$

A schematic representation of the division of the unit cell employed in the PAW method is shown in Figure 3.4.

The linear transformation within each augmentation region Ω_a is defined by specifying a set of functions, $\{\phi_i^a\}$, which form a complete basis set within Ω_a. This set of functions serves as a basis set for the expansion of the true electronic wave function in each augmentation region with coefficients c_i^a:

$$|\psi\rangle = \sum_i c_i^a |\phi_i^a\rangle \quad \text{in} \quad \Omega_a. \tag{3.34}$$

A possible and natural choice for the basis set $\{\phi_i^a\}$ are the solutions of the radial Schrödinger equation for the isolated atom. In this case the index i is a contracted notation for the atomic position $\mathbf{R}_a$, the angular momentum quantum numbers (l, m), and an additional index n used to label solutions with different energy. The final expression for the linear transformation is given by [61, 63]

$$\hat{T} = \hat{1} + \sum_a \sum_i (|\phi_i^a\rangle - |\tilde{\phi}_i^a\rangle)\langle \tilde{p}_i^a|. \tag{3.35}$$

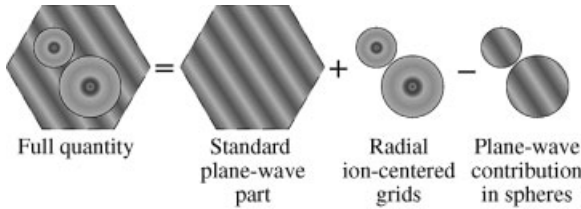| Full quantity | Standard plane-wave part | Radial ion-centered grids | Plane-wave contribution in spheres |

Figure 3.4 (online color at: www.pss-b.com) Schematic representation of the division of the unit cell employed in the PAW method.

where the auxiliary pseudo partial waves $|\tilde{\phi}_i^a\rangle$ equal the AE counterparts $|\phi_i^a\rangle$ beyond the radius r_c^a of the PAW sphere, and are used to expand the pseudized function $|\tilde{\psi}\rangle$ inside the augmentation sphere. The atom-centered projector functions $|\tilde{p}_i^a\rangle$ are strictly localized inside the spheres and obey the orthogonality property:

$$\langle \tilde{p}_i^a | \tilde{\phi}_j^a \rangle = \delta_{ij}. \tag{3.36}$$

The matrix elements of a local or semilocal operator $\hat{A}$ between two AE wave functions can be efficiently and accurately evaluated by employing the linear transformation $\hat{\mathcal{T}}$ given in Eq. (3.35). After some algebra one obtains:

$$\langle \psi | \hat{A} | \psi \rangle = \langle \tilde{\psi} | \hat{A} | \tilde{\psi} \rangle + \sum_{ij} \langle \tilde{\psi} | \tilde{p}_i \rangle [\langle \phi_i | \hat{A} | \phi_j \rangle - \langle \tilde{\phi}_i | \hat{A} | \tilde{\phi}_j \rangle] \langle \tilde{p}_j | \tilde{\psi} \rangle. \tag{3.37}$$

The first term in Eq. (3.37) has the same mathematical structure as the expression present in the PP formalism. As it involves only the "smooth" part of the wave function, it can be evaluated either in real or reciprocal space, depending on the nature of $\hat{A}$, by changing representation through fast Fourier transform techniques. The second term involves the onsite matrix elements of the $\hat{A}$ operator between AE and pseudo partial waves. It can be evaluated either by employing radial and angular meshes in real space or by expanding the operator $\hat{A}$ in terms of angular momenta.

Within the PAW formalism, the oscillator strengths, – i.e., the basic ingredients required to evaluate $P^0(\omega)$, and the matrix elements of $\Sigma(\omega)$ – can be obtained by means of the following equation [64]:

$$\langle \psi_{b\mathbf{k}-\mathbf{q}} | e^{-i(\mathbf{q}+\mathbf{G}) \cdot \mathbf{r}} | \psi_{b'\mathbf{k}} \rangle = \langle \tilde{\psi}_{b\mathbf{k}-\mathbf{q}} | e^{-i(\mathbf{q}+\mathbf{G}) \cdot \mathbf{r}} | \tilde{\psi}_{b'\mathbf{k}} \rangle + \sum_{ij} \langle \tilde{\psi}_{b\mathbf{k}-\mathbf{q}} | \tilde{p}_i \rangle \langle \tilde{p}_j | \tilde{\psi}_{b'\mathbf{k}} \rangle e^{-i(\mathbf{q}+\mathbf{G}) \cdot \mathbf{R}_i}$$

$$\times \left[\langle \phi_i | e^{-i(\mathbf{q}+\mathbf{G}) \cdot (\mathbf{r}-\mathbf{r}_i)} | \phi_j \rangle - \underbrace{\langle \tilde{\phi}_i | e^{-i(\mathbf{q}+\mathbf{G}) \cdot (\mathbf{r}-\mathbf{r}_i)} | \tilde{\phi}_j \rangle}_{} \right]$$

$$\times 4\pi \sum_{lm} (-i)^l \widehat{\mathcal{Y}_m^l(\mathbf{q}+\mathbf{G})} \, G_{l_i m_i l_j m_j}^{lm} \int j_l(|\mathbf{q}+\mathbf{G}|r)(\phi_{n_i l_i} \phi_{n_j l_j} - \tilde{\phi}_{n_i l_i} \tilde{\phi}_{n_j l_j}) d\mathbf{r} \, , \tag{3.38}$$

where the plane wave has been expressed in terms of Bessel functions $j_l(x)$ and real spherical harmonics $\mathcal{Y}_m^l(\hat{\mathbf{G}})$ via the Rayleigh expansion. The symbol $G_{l_i m_i l_j m_j}^{lm}$ is used to denote the Gaunt coefficient [65], defined by:

$$G_{l_i m_i l_j m_j}^{lm} = \int \mathcal{Y}_{m_i}^{l_i} \mathcal{Y}_m^l \mathcal{Y}_{m_j}^{l_j} d\Omega. \tag{3.39}$$

3.4
QP Corrections to the BOs at Interfaces

In the DFT approach, the valence and conduction band offsets (VBO and CBO, respectively) are conveniently split into two terms:

$$\text{VBO} = \Delta E_v^{\text{DFT}} + \Delta V, \tag{3.40}$$

$$\text{CBO} = \Delta E_c^{\text{DFT}} + \Delta V. \tag{3.41}$$

The first term ΔE_v^{DFT} (resp. ΔE_c^{DFT}) on the right-hand side of Eq. (3.40) [resp. Eq. (3.41)] is referred to as the *band-structure contribution*. It is defined as the difference between the valence band maximum (VBM) (and the conduction band minimum (CBM), respectively) *relative to the average of the electrostatic potential in each material*. These are obtained from two independent standard bulk calculations on the two interface materials. Alternatively, these can be obtained from an analysis of the local density of states [66]. The second term ΔV, called the *lineup of the average of the electrostatic potential* across the interface, accounts for all the intrinsic interface effects. It is determined from a supercell calculation with a model interface.

Despite the limitations of DFT in finding accurate eigenenergies, the VBOs are often obtained with a very good precision, in particular for semiconductors [67]. This has opened an indirect route to computing the CBOs through the experimental band gaps using:

$$\text{CBO} = \Delta E_g^{\text{exp}} + \text{VBO}. \tag{3.42}$$

Note that this equation is equivalent to applying a scissor correction to the conduction bands on both sides of the interface, as can be seen by inserting Eqs. (3.40) and (3.42):

$$\text{CBO} = \Delta E_c^{\text{DFT}} + \Delta V + \left(\Delta E_g^{\text{exp}} - \Delta E_g^{\text{DFT}}\right), \tag{3.43}$$

and then comparing with Eq. (3.41).

The first QP calculation of the band-offsets (BOs) goes back to the work of Zhang *et al.* [68] who were investigating the VBO at the AlAs−GaAs(001) interface. They assumed that the lineup of the potential ΔV is already well described within DFT, arguing that QP corrections would not affect ΔV since it only depends on the long range electrostatic potentials. The latter are well-known functions of the electronic densities, which are given quite accurately by DFT.

Recently, the many-body effects on ΔV have been explicitly investigated [69]. This was done by comparing the electronic density and the resulting ΔV calculated within DFT and QSGW for a small model of the Si/SiO$_2$ interface illustrated in Figure 3.5(a). It was found that the QSGW results differ only slightly from DFT. The change in planar average of the electronic density, $\overline{\varrho}$, was at most 1 me/a.u. in the interface region, as illustrated in Figure 3.5(b). This lead to a variation in the macroscopic average of the local potential $\overline{V}$ [Figure 3.5(c)] smaller than 45 meV in that region. However, the net difference between the bulk materials, which is relevant for the lineup of the potential ΔV, was less than 12 meV. It was thus concluded that the interfacial charge density and, consequently, the associated dipole moments are well described within DFT, justifying the assumption that the lineup of the potential can be taken to be the same as in DFT. For metal-insulator or metal-semiconductor interfaces, this assumption still needs to be carefully checked.
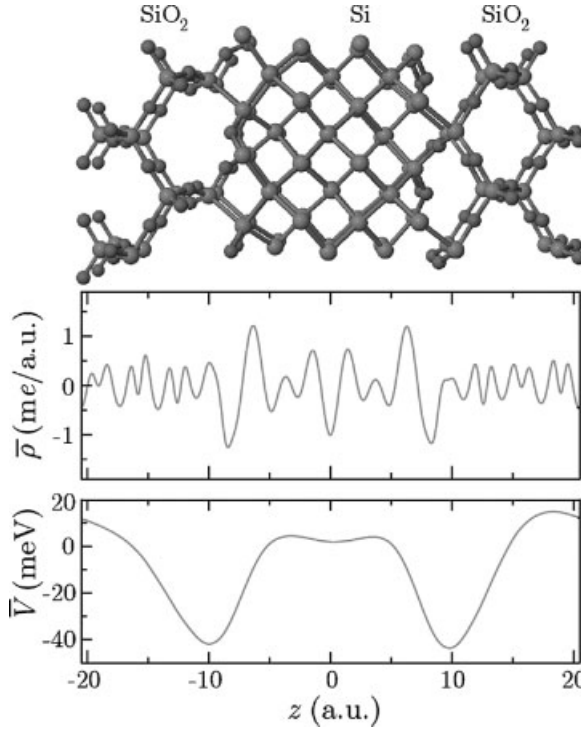
Figure 3.5 (online color at: www.pss-b.com) Small model of the Si/SiO$_2$ interface (upper panel) used in Ref. [69] to compute the difference between DFT and QSGW for the planar average of the electronic density $\overline{\varrho}$ (middle panel) and the macroscopic average of the local potential $\overline{V}$ (lower panel). The density and the potential are expressed in me/a.u. and in meV, respectively.

Assuming that ΔV can be taken from DFT, only the band-structure contribution is modified by QP corrections:

$$\text{VBO} = \Delta E_v^{\text{QP}} + \Delta V = \Delta E_v^{\text{DFT}} + \Delta(\delta E_v) + \Delta V, \tag{3.44}$$

$$\text{CBO} = \Delta E_c^{\text{QP}} + \Delta V = \Delta E_c^{\text{DFT}} + \Delta(\delta E_c) + \Delta V, \tag{3.45}$$

where $\delta E_v = E_v^{\text{QP}} - E_v^{\text{DFT}}$ (resp. $\delta E_c = E_c^{\text{QP}} - E_c^{\text{DFT}}$) is the QP correction at the VBM (resp. CBM) and $\Delta(\delta E_v)$ [resp. $\Delta(\delta E_c)$] is the corresponding difference between the two materials. It is important to stress that these corrections, which are obtained from bulk calculations, are the only additional ingredients that are required when DFT calculations of the VBO and CBO already exist.

Interestingly, for various semiconductor interfaces, the QP corrections of the band edges are found to be almost the same on both sides [68, 70] leading to $\Delta(\delta E_v) \leq$ 0.2 eV in Eq. (3.44). As a result of this cancellation of errors, DFT is quite successful

for these interfaces [67] with errors ranging from 0.1 to 0.5 eV, despite the limitations mentioned above. This relative success of DFT explains why it has been widely used to predict the VBO for a wide range of interfaces. And, when needed, the CBO was also predicted using a simple scissor operator to correct the band gap to the experimental value. This assumption was further motivated by the fact that MBPT calculations going beyond GW by including an approximate vertex correction ($GW\Gamma$) showed that the VBM remained at its DFT value for silicon, with the whole correction going to the conduction bands [30, 71].

However, when it comes to semiconductor–insulator or insulator–insulator interfaces, it appears that the errors to the VBO can be much more important in DFT. For instance, for the Si/SiO_2 interface, the VBOs are calculated to be 2.3–3.3 eV [66, 72–74] in noticeable disagreement with the experimental results of 4.3 eV [75, 76]. In contrast, for the Si/ZrO_2 and Si/HfO_2 interfaces, the calculated VBOs for the stable insulating O-terminated interfaces are around 2.5–3 eV [77–81], in reasonable agreement with experiment (2.7–3.4 eV) [82–90]. For these interfaces, scissor-corrected DFT has also been used to predict CBOs of about 1.7–2.2 eV, which compare quite well with the experimental values (1.5–2 eV) [87–90]. It seems that the cancellation of errors may vary strongly from one system to another, emphasizing the need to go beyond DFT by including QP corrections. Interestingly, hybrid functionals have been shown to give very good VBOs and CBOs compared to experiment for both the Si/SiO_2 and Si/HfO_2 interfaces by tuning the fraction of HF exchange for each bulk component to reproduce the experimental value of the band gap [9, 10].

For the Si/ZrO_2 interface, a QP correction of about 1.1 eV to the VBOs has been extracted from GW calculations for Si [70] and ZrO_2 [91] and used together with the experimental band gap to correct DFT BOs in several works [92, 93]. For the Si/HfO_2 interface, the same correction as for Si/ZrO_2 has been adopted [94] since there were no GW calculations available for HfO_2. Such an assumption seems quite reasonable given the analogous electronic structure of ZrO_2 and HfO_2. However, for both Si/ZrO_2 and Si/HfO_2 interfaces, the VBOs obtained by applying this correction are too large (and as a consequence the CBOs too small) with respect to the available experiments [92–94].

This discrepancy can be traced back to the fact that, while the QP corrections to the gap δE_g are *not* very sensitive to the choice of the PPM [64], the absolute values of δE_v and δE_c *may vary from one PPM to another*, as reported in Refs. [69, 95]. The results of Ref. [69] for Si and c-SiO_2 and those of Ref. [95] for c-ZrO_2 are summarized in Table 3.1. Since a precise knowledge of the QP corrections at the band edges is required for BO calculations, *it is necessary to go beyond PPMs*, by taking the frequency dependence of W into account explicitly. This can be done by using the CD method (see Section 2.3). The comparison between the CD and PPM results for a given system allows one to validate a PPM for further study of similar systems. Interestingly, the PPM proposed by GN [45] seems to lead to QP corrections in excellent agreement with those of the CD method (see Table 3.1), at variance with the other PPMs. Further investigation is still required to generalize this finding.

Table 3.1 QP corrections (in eV) at the VBM (δE_v), at the CBM (δE_c), and for the band gap (δE_g) for Si, c-SiO$_2$ (from Ref. [69]), and c-ZrO$_2$ (from Ref. [95]). The corrections are calculated within e-QSGW using the PPMs proposed by HL [31], vdLH [49], GN [45], EF [50], and without PPM using the CD method.

		HL	GN	vdLH	EF	CD
Si	δE_v	−0.6	−0.4	−0.6	−0.6	−0.4
	δE_c	+0.1	+0.2	+0.1	+0.1	+0.2
	δE_g	+0.7	+0.6	+0.7	+0.7	+0.6
c-SiO$_2$	δE_v	−2.6	−2.0	−2.5	−2.3	−1.9
	δE_c	+1.3	+1.5	+1.1	+1.2	+1.5
	δE_g	+3.9	+3.5	+3.6	+3.5	+3.4
c-ZrO$_2$	δE_v	−1.1	−0.5	–	–	−0.7
	δE_c	+1.3	+1.4	–	–	+1.4
	δE_g	+2.4	+1.9	–	–	+2.1

It is important to note that, rigorously, the QP corrections on the BOs should be calculated using the same PPs and the same exchange-correlation approximation as for the interface calculations. Indeed, the QP corrections are much more sensitive to these approximations than the band gap. Therefore, extreme caution should be applied when the QP corrections to DFT BOs are not calculated using the same approximations (e.g., in the PP, the exchange-correlation approximation, and the PPM).

Once this is carefully taken into account, the QP corrections can be calculated. It is also interesting to analyze the effect of including vertex corrections. The results reported in Ref. [69] for Si and c-SiO$_2$, and in Ref. [96] for c-HfO$_2$, are summarized in Table 3.2. While e-QSGW leads to a lowering of the VBM of Si compared to the DFT result ($\delta E_v \leq 0$), the inclusion of vertex corrections brings it back to roughly its original value with a small shift upwards of 0.1 eV, with all of the QP correction being on the conduction band. A similar result was also found previously [30, 71]. For HfO$_2$, the vertex correction acts in the same way though in this case the shift to the VBM is slightly larger (0.2 eV downwards). The results for Si and c-HfO$_2$ give some motivation to the use of a scissor operator to compute the CBO within DFT. However, for c-SiO$_2$, the results are very different. First, the VBM is also raised when including the vertex, but it definitely does not regress to the DFT level. This indicates that in Si and c-HfO$_2$, the recovery of the DFT VBM with the vertex is a coincidence. It also definitely rules out the use of a simple scissor operator for the computation of the BOs, unless further checks or refinements are made.

Finally, using Eqs. (3.44) and (3.45), the BOs can be computed within MBPT at the GW and $GW\Gamma$ levels. The results reported in Refs. [69, 95] compare very well with the experimental ones. Within e-QSGW the agreement is excellent for both the VBO and CBO (less than 0.3 eV difference). The effect of the vertex correction is less than 0.1 eV on the BOs. This results from a cancellation of the effects on each side of the interface. Indeed, in Eqs. (3.44) and (3.45), it is the difference between the QP corrections in both materials [$\Delta(\delta E_v)$ and $\Delta(\delta E_c)$] that matters. As

Table 3.2 QP corrections (in eV) at the VBM (δE_v), at the CBM (δE_v), and for the band gap (δE_g) for Si, c-SiO$_2$ (from Ref. 69), and c-HfO$_2$ (from Ref. [96]). The corrections are calculated using e-QSGW and e-QSG$W\Gamma$ (the e-QS are omitted below).

	Si		c-SiO$_2$		c-HfO$_2$	
	GW	$GW\Gamma$	GW	$GW\Gamma$	GW	$GW\Gamma$
δE_v	-0.4	$+0.1$	-1.9	-1.3	-0.6	-0.2
δE_c	$+0.2$	$+0.7$	$+1.5$	$+1.8$	$+1.1$	$+1.6$
δE_g	$+0.6$	$+0.6$	$+3.4$	$+3.1$	$+1.7$	$+1.8$

can be seen in Table 3.2, this difference is typically less than 0.1 eV for the couples Si/SiO$_2$ and Si/HfO$_2$.

The effect of the vertex correction is very small compared to standard GW calculations. For the homogenous electron gas and atomic systems, it has been shown [97] that the local vertex correction of Del Sole et al. generally causes a large unphysical upward shift in the absolute values of band energies (and total energies). However, the relative changes in the QP energies obtained using $G_0 W_0 \Gamma$ are very small compared to $G_0 W_0$ results. The large shift can be attributed to an unphysical feature of the spectral function of the self-energy, which can come to have the wrong sign after a given energy. In the absence of non-trivial external electromagnetic fields, the spectral function of Σ should be strictly positive (negative) definite for frequencies below (above) the Fermi energy. A demonstration of this failure for the homogenous electron gas is given in Figure 3.6.
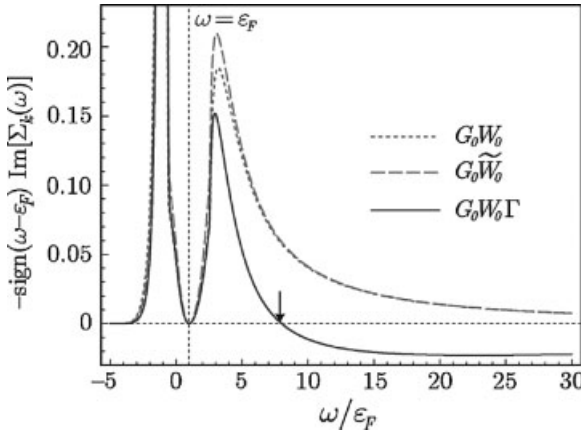

Figure 3.6 (online color at: www.pss-b.com) The imaginary part of the self-energy in jellium for $r_s = 2.0$ and $k = 0.5 k_F$. This is the spectral function of Σ. Plotted in this way, it should be positive definite everywhere. The curve for $G_0 W_0 \Gamma$ fails to be positive definite from the inset arrow onwards, after which it goes to a negative minimum and then slowly decays back to zero. The spectral function from $G_0 \tilde{W}_0$, in contrast, has no such behavior and has the proper limit.

In contrast, as can also be seen from Figure 3.6, there is no such failure for the implementation of the vertex only in the screened interaction, i.e., $G_0 \widetilde{W}_0$. Ironically, this is actually more time-consuming to implement in any existing code, as it requires an extra matrix multiplication before the calculation of the dielectric matrix. However, the bandwidth of metals compares better to experiments with this implementation, and it has also recently been used in Bethe-Salpeter calculations on molecules and metal clusters to good effect [98, 99]. These results indicate that the $G_0 \widetilde{W}_0$ vertex might yield better BOs, and the utility of this type of simple vertex correction certainly merits further study.

3.5
QP Corrections for Defects

Despite the methodological advancements discussed in previous sections it is still computationally challenging to compute total energies in GW and MBPT and no calculation for a defect has been reported so far.

The conventional way of obtaining defect formation energies, namely by calculating the total energy difference between the defective and a reference system [100], is therefore unavailable. Defect formation energies become accessible in GW again by realizing that QP energies correspond to electron addition and removal energies. Since the ionization potential and the electron affinity can be expressed in terms of total energy differences the formation energy of a defect can be formally rewritten as the successive charging of a lower (or if more convenient, higher) charge state [101, 102].

The formation of a neutral and a positive from a 2+ charge state is depicted schematically in Figure 3.7. For the example of the positive charge state this process reads mathematically

$$E_D^f(+, \varepsilon_F) = \Delta(+, \boldsymbol{R}_+^D, \boldsymbol{R}_{2+}^D) + A(2+, \boldsymbol{R}_{2+}^D) \\ + E_D^f(2+, \varepsilon_F = 0) + \varepsilon_F, \tag{3.46}$$
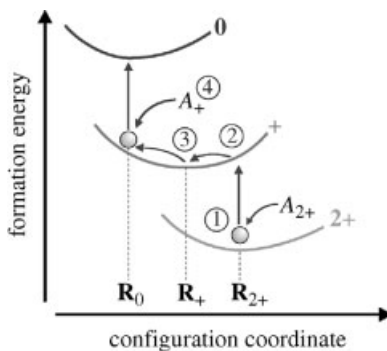

Figure 3.7 (online color at: www.pss-b.com) Formation of the neutral Si_i from the 2+ charge state. A_+ and A_{2+} are short for the electron affinities $A(+, \boldsymbol{R}_0)$ and $A(2+, \boldsymbol{R}_{2+})$ (see text), respectively, and $\boldsymbol{R}_q$ denotes the atomic positions in charge state q.

where $E_D^f(+, \varepsilon_F)$ and $E_D^f(2+, \varepsilon_F = 0)$ are the formation energies of the $+$ and 2+ and ε_F the Fermi energy. $\boldsymbol{R}_q^D$ denotes the atomic coordinates of defect D in charge state q. $A(2+, \boldsymbol{R}_{2+}^D)$ defines the vertical electron affinity of the 2+ state $E(+, \boldsymbol{R}_{2+}^D) - E(2+, \boldsymbol{R}_{2+}^D)$ (step 1 in Figure 3.7), referenced to the top of the valence band, whereas $\Delta(+, \boldsymbol{R}_+^D, \boldsymbol{R}_{2+}^D)$ gives the subsequent relaxation energy in the positive charge state $E(+, \boldsymbol{R}_+^D) - E(+, \boldsymbol{R}_{2+}^D)$ (step 2). The formation energy of higher charge states follows analogously.

Having split the formation energy into an electron addition and a lattice part, the most suitable computational technique can be employed for each part. For electron affinities (change in charge state at fixed geometry) we apply the GW approach. For relaxation energies (change of geometry in the same charge state) we retain DFT. Since the scheme has to be anchored on the formation energy of at least one charge state that cannot be corrected by GW (the 2+ in our example) the GW-correction approach depends on the quality of this formation energy and its associated valence band maximum (the reference for the Fermi energy). This is a weakness of the scheme and implies that relative formation energies (i.e., charge transition levels for which this dependence cancels exactly) are more accurate than absolute formation energies.

Applied to the self-interstitial in silicon the GW scheme corrects the DFT-LDA formation energy of different neutral configurations (see Figure 3.8) by $\sim$1.1 eV [102] in good agreement with diffusion Monte Carlo calculations [103, 104]. For the $+ \rightarrow 0$ charge transition level of a phosphor vacancy at the InP(110) surface the GW-corrected value of 0.82 eV is in much better agreement with the experimental value of 0.75 ± 0.1 eV than the DFT-LDA charge transition level of
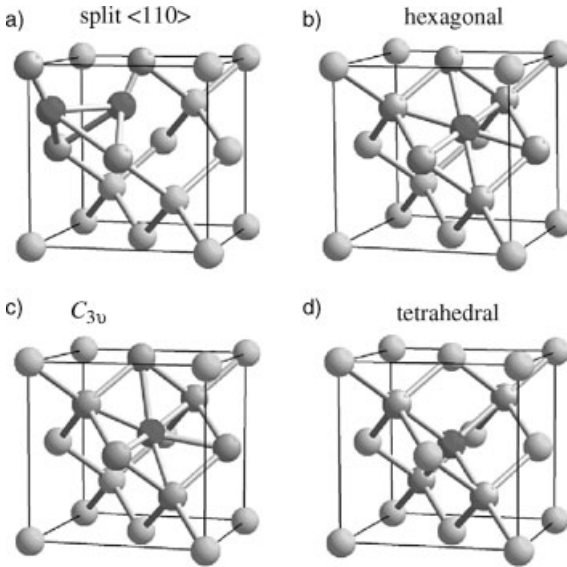

Figure 3.8 (online color at: www.pss-b.com) (a) Split $<110>$, (b) hexagonal, (c) C_{3v}, and (d) tetrahedral configuration of the Si_i. Defect atoms are shown in red and nearest neighbors in gray.

0.47 eV [101]. A long-standing problem was solved for silicon dioxide, where DFT-LDA favors the diffusion of charged oxygen interstitials, in clear disagreement with available experimental results. Agreement with experiment is recovered by applying the $G_0 W_0$-correction approach, which substantially increases the formation energies of the negatively charged interstitials, leaving as dominant self-diffusion mechanism the neutral one [105].

The decomposition presented in the previous paragraphs supposes that the electronic states calculated in GW correspond to total energy differences. At present this assumption is not verifiable numerically, because GW total energies cannot be calculated for the defect systems at hand. The lowest excitation energies can, however, be expressed in two different ways. The electron affinities that enter in our discussion above can alternatively be seen as the ionization potential of a system with one extra electron:

$$I_0 = E_D(+) - E_D(0) = A_+. \tag{4.47}$$

While excitation energies calculated with the exact self-energy would satisfy Eq. (4.47) those from approximate self-energies – like GW – do not. This is shown in Figure 3.9 for the C split interstitial in silicon carbide (3C-SiC) in the neutral geometry. The first red dashed line is the electron affinity of the interstitial in the 2+ charge state (A_{2+}), while the second red dashed line corresponds to the ionization potential of the + charge state (I_+). If Eq. (4.47) was satisfied in these GW defect calculations the two lines would be equal. Instead they differ by 0.19 eV [106]. The excitations A_+ and I_0 (represented by the orange dashed lines) differ by 0.25 eV. This is not much, but noticeable.
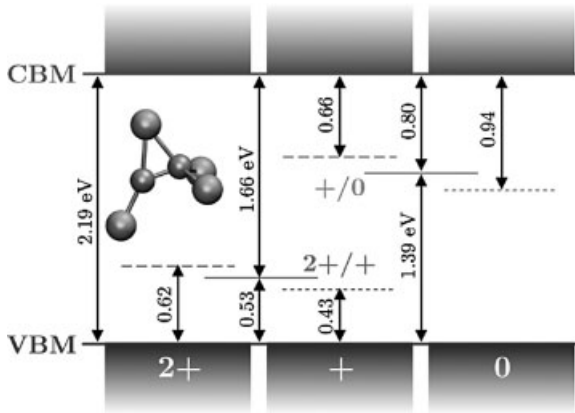

Figure 3.9 (online color at: www.pss-b.com) Defect level position for C split interstitial in 3C-SiC evaluated within *GW* for different charge states (2+, +, and 0). The atomic structure is fixed to the geometry of the neutral state (see inset). The occupied levels are depicted as a dotted line, the empty ones as a dashed line, and their mid values as a solid line. The transition energy is indicated in red for 2+ / + and in orange for + /0.

How can we reconcile this discrepancy? Slater [107] already identified this issue in the 1970s in DFT and HF calculations. He proposed to consider the total energy as a continuous function of electron number and to expand up to second order between integral numbers of electrons. The total energy difference in Eq. (4.47) can then be written as the energy of the highest occupied (or lowest unoccupied) state at half occupation. Equivalently, one could write this as the mean value between the energy of the highest occupied state of the neutral system and the energy of the lowest unoccupied state of a positively charged system. Since GW calculations at half occupation are not straightforward, the latter is more applicable. For the point defect from Figure 3.9 this then gives the following transition energies $E_{GW}(2+/+) = E_v + 0.53\,\text{eV}$ and $E_{GW}(+/0) = E_c - 0.80\,\text{eV} = E_v + 1.39$ eV. We see that the last equality only holds when performing the mean value technique, which reconciles the slight discrepancy between total energies and QP levels that exists in the GW formalism.

3.6
Conclusions and Prospects

The improvements discussed in this review are now available in several popular simulation packages, and have increased the speed of MBPT calculations. This has enabled the study of larger systems and more complex problems, such as interfaces and defects. We have illustrated this by presenting some recent MBPT results, while trying to highlight the main difficulties and caveats. It is to be expected that many more calculations on interfaces and defects relying on MBPT will follow.

As a final remark, it should be mentioned that DFT (or popular flavors of DFT) may fail to predict the correct geometry of certain interfaces or defects. In such cases, the energy levels (be it the VBM, the CBM, or defect levels) computed from MBPT could also be wrong. In order to avoid such problems, it is highly desirable to be able to compute the energy and the forces self-consistently from many-body theories for supercells ranging from 100 to 200 atoms. This is an important aim of future developments in MBPT implementations.

References

1 Capasso, F. and Magaritondo, G. (eds) (1987) *Heterojunction Band Discontinuities: Physics and Device Applications*, North-Holland, Amsterdam.

2 Sze, S.M. and Ng, K.K. (2007) *Physics of Semiconductor Devices*, 3rd edn, John Wiley & Sons, New York.

3 Fleetwood, D.M., Pantelides, S.T., and Schrimpf, R.D.C. (eds) (2008) *Defects in Microelectronic Materials and Devices*, CRC Press, Boca Raton, Florida.

4 Wada, K. and Pang, S.W. (eds) (2001) *Defects in Optoelectronic Materials*, CRC Press, Boca Raton, Florida.

5 Gusev, E. (ed.) (2006) *Defects in High-k Gate Dielectric Stacks*, Springer, Dordrecht, The Netherlands.

6 Knaup, J.M., Deák, P., Frauenheim, Th., Gali, A., Hajnal, Z., and Choyke, W.J. (2005) *Phys. Rev. B*, **72**, 115323.

7 Xiong, K., Robertson, J., Gibson, M.C., and Clark, S.J. (2005) *Appl. Phys. Lett.*, **87**, 183505.

8 Broqvist, P. and Pasquarello, A. (2007) *Microelectron. Eng.*, **84**, 2022.

9 Broqvist, P., Alkauskas, A., and Pasquarello, A. (2008) *Appl. Phys. Lett.*, **92**, 132911.

10 Akauskas, A., Broqvist, P., Devynck, F., and Pasquarello, A. (2008) *Phys. Rev. Lett.*, **101**, 106802.

11 Alkauskas, A., Broqvist, P., and Pasquarello, A. (2008) *Phys. Rev. Lett.*, **101**, 046405.

12 Curtiss, L.A., Redfern, P.C., Raghavachari, K., and Pople, J.A. (1998) *J. Chem. Phys.*, **109**, 42.

13 Muscat, J., Wander, A., and Harrison, N.M. (2001) *Chem. Phys. Lett.*, **342**, 397.

14 Paier, J., Marsman, M., Hummer, K., Kresse, G., Gerber, I.C., and Ángyán, Th. (2006) *J. Chem. Phys.*, **124**, 154709; (2006) *J. Chem. Phys.*, **125**, 249901.

15 Ernzerhof, M., Perdew, J.P., and Burke, K. (1997) *Int. J. Quantum Chem.*, **64**, 285.

16 Ernzerhof, M. and Scuseria, G. (1999) *J. Chem. Phys.*, **110**, 5029.

17 Kümmel, S. and Kronik, L. (2008) *Rev. Mod. Phys.*, **80**, 3.

18 Hedin, L. and Lundqvist, S. (1969) *Solid State Physics*, vol. **23** (eds H. Ehrenreich, F. Seitz, and D. Turnbull), Academic Press, New York, p. 1.

19 Fetter, A.L. and Walecka, J.D. (1971) *Quantum Theory of Many-Particle Systems*, McGraw-Hill, New York.

20 Abrikosov, A.A., Gorkov, L.P., and Dzyaloshinskii, E. (1975) *Methods of Quantum Field Theory in Statistical Physics*, Dover, New York.

21 Landau, L.D. and Lifschitz, E.M. (1980) *Statistical Physics Part II*, Pergamon, Oxford.

22 Onida, G., Reining, L., and Rubio, A. (2002) *Rev. Mod. Phys.*, **74**, 601.

23 Hedin, L. (1965) *Phys. Rev. A*, **139**, 796.

24 Nelson, W., Bokes, P., Rinke, P., and Godby, R.W. (2007) *Phys. Rev. A*, **75**, 032505.

25 Romaniello, P., Guyot, S., and Reining, L. (2009) *J. Chem. Phys.*, **131**, 154111.

26 Godby, R.W., Schlüter, M., and Sham, L.J. (1986) *Phys. Rev. Lett.*, **56**, 2415.

27 Aulbur, W.G., Jonsson, L., and Wilkins, J.W. (2000) *Solid State Phys.*, **54**, 1.

28 Rinke, P., Qteish, A., Neugebauer, J., Freysoldt, C., and Scheffler, M. (2005) *New J. Phys.*, **7**, 126.

29 Rinke, P., Qteish, A., Neugebauer, J., and Scheffler, M. (2008) *Phys. Status Solidi B*, **245**, 929.

30 Del Sole, R., Reining, L., and Godby, R.W. (1994) *Phys. Rev. B*, **49**, 8024.

31 Hybertsen, M.S. and Louie, S.G. (1986) *Phys. Rev. B*, **34**, 5390.

32 Li, J.-L., Rignanese, G.-M., and Louie, S.G. (2005) *Phys. Rev. B*, **71**, 193102.

33 White, I.D., Godby, R.W., Rieger, M.M., and Needs, R.J. (1997) *Phys. Rev. Lett.*, **80**, 4265.

34 Rohling, M., Wang, N.P., Krüger, P., and Pollmann, J. (2003) *Phys. Rev. Lett.*, **91**, 256802.

35 Pulci, O., Reining, L., Onida, G., Del Sole, R., and Bechstedt, F. (2001) *Comput. Mater. Sci.*, **20**, 300.

36 Rinke, P., Delaney, K., García-González, P., and Godby, R.W. (2004) *Phys. Rev. A*, **70**, 063201.

37 Bruneval, F., Vast, M., and Reining, L. (2006) *Phys. Rev. B*, **74**, 045102.

38 Rieger, M.M., Steinbeck, L., White, I.D., Rojas, H.N., and Godby, R.W. (1999) *Comput. Phys. Commun.*, **117**, 211.

39 Holm, B. and von Barth, U. (1998) *Phys. Rev. B*, **57**, 2108.

40 Schöne, W.-D. and Eguiluz, A.G. (1998) *Phys. Rev. Lett*, **81**, 1662.

41 Ku, W. and Eguiluz, A.G. (2002) *Phys. Rev. Lett.*, **89**, 126401.

42 Faleev, S.V., van Schilfgaarde, M., and Kotani, T. (2004) *Phys. Rev. Lett.*, **93**, 126406.

43 van Schilfgaarde, M., Kotani, T., and Faleev, S.V. (2006) *Phys. Rev. Lett.*, **96**, 226402.

44 Kotani, T., van Schilfgaarde, M., and Faleev, S.V. (2007) *Phys. Rev. B*, **76**, 165106.

45 Godby, R.W. and Needs, R.J. (1989) *Phys. Rev. Lett.*, **62**, 1169.

46 Ashcroft, N.W. and Mermin, N.D. (1976) *Solid State Physics*, Cornell University Press, Ithaca, New York.

47 Johnson, D.L. (1974) *Phys. Rev. B*, **9**, 4475.

48 Taut, M. (1985) *J. Phys. C*, **18**, 2677.

49 von der Linden, W. and Horsch, P. (1988) *Phys. Rev. B*, **37**, 8351.

50 Engel, G.E. and Farid, B. (1993) *Phys. Rev. B*, **47**, 15931.

51 Lundqvist, B.I. (1968) *Phys. Kondens. Mater.*, **7**, 117.

52 Bruneval, F. and Gonze, X. (2008) *Phys. Rev. B*, **78**, 085125.

53 Anglade, P.-M. and Gonze, X. (2008) *Phys. Rev. B*, **78**, 045126.

54 Kotani, T. and van Schilfgaarde, M. (2002) *Solid State Commun.*, **121**, 461.

55 Gómez-Abal, R., Li, X., Scheffler, M., and Ambrosch-Draxl, C. (2008) *Phys. Rev. Lett.*, **101**, 106404.

56 Marini, A., Onida, G., and Del Sole, R. (2001) *Phys. Rev. Lett.*, **88**, 016403.

57 Delaney, K., García-González, P., Rubio, A., Rinke, P., and Godby, R.W. (2004) *Phys. Rev. Lett.*, **93**, 249701.

58 Tiago, M.L., Ismail-Beigi, S., and Louie, S.G. (2004) *Phys. Rev. B*, **69**, 125212.

59 Rohlfing, M., Krüger, P., and Pollmann, J. (1995) *Phys. Rev. Lett.*, **75**, 3489.

60 Jiang, H., Gómez-Abal, R., Rinke, P., and Scheffler, M. (2009) *Phys. Rev. Lett.*, **102**, 126403.

61 Blöchl, P.E. (1994) *Phys. Rev. B*, **50**, 17953.

62 Hamann, D.R., Schlüter, M., and Chiang, C. (1979) *Phys. Rev. Lett.*, **43**, 1494.

63 Torrent, M., Jollet, F., Bottin, F., Zerah, G., and Gonze, X. (2008) *Comput. Mater. Sci.*, **42**, 337.

64 Arnaud, B. and Alouani, M. (2000) *Phys. Rev. B*, **62**, 4464.

65 Rotenber, M., Bivins, R., Metropolis, N., and Wooten, J.K. (1959) *The 3-j and 6-j Symbols* Technology Press, Massachusetts Institute of Technology, Cambridge.

66 Yamasaki, T., Kaneta, C., Uchiyama, T., Uda, T., and Terakura, K. (2001) *Phys. Rev. B*, **63**, 115314.

67 Van de Walle, C.G. and Martin, R.M. (1987) *Phys. Rev. B*, **35**, 8154.

68 Zhang, S.B., Tománek, D., Louie, S.G., Cohen, M.L., and Hybertsen, M.S. (1988) *Solid State Commun.*, **66**, 585.

69 Shaltaf, R., Rignanese, G.-M., Gonze, X., Giustino, F., and Pasquarello, A. (2008) *Phys. Rev. Lett.*, **100**, 6401.

70 Zhu, X. and Louie, S.G. (1991) *Phys. Rev. B*, **43**, 14142.

71 Fleszar, A. and Hanke, W. (1997) *Phys. Rev. B*, **56**, 10228.

72 Watarai, M., Nakamura, J., and Natori, A. (2004) *Phys. Rev. B*, **69**, 035312.

73 Tuttle, B.R. (2004) *Phys. Rev. B*, **70**, 125322.

74 Giustino, F. and Pasquarello, A. (2005) *Surf. Sci.*, **586**, 183.

75 Keister, J.W., Rowe, J.E., Kolodziej, J.J., Niimi, H., Madey, T.E., and Lucovsky, G. (1999) *J. Vac. Sci. Technol. B*, **17**, 1831.

76 Afanas'ev, V.V., Houssa, M., and Stesman, A. (2001) *Appl. Phys. Lett.*, **78**, 3073.

77 Peacock, P.W. and Robertson, J. (2004) *Phys. Rev. Lett.*, **92**, 057601.

78 Peacock, P.W., Xiong, K., Tse, K.Y., and Robertson, J. (2006) *Phys. Rev. B*, **73**, 075328.

79 Puthenkovilakam, R., Carter, E.A., and Chang, J.P. (2004) *Phys. Rev. B*, **69**, 155329.

80 Puthenkovilakam, R. and Chang, J.P. (2004) *J. Appl. Phys.*, **96**, 2701.

81 Chen, G.H., Hou, Z.F., and Gong, X.G. (2009) *Appl. Phys. Lett.*, **95**, 102905.

82 Miyazaki, S., Narasaki, M., Ogasawara, M., and Hirose, M. (2001) *Microelectron. Eng.*, **59**, 373.

83 Oshima, M., Toyoda, S., Okumura, T., Okabayashi, J. Kumigashira, H. Ono, K., Niwa, M., Usuda, K., and Hirashita, N. (2003) *Appl. Phys. Lett.*, **83**, 2172.

84 Wang, S.J., Huan, A.C.H., Foo, Y.L., Chai, J.W., Pan, J.S., Li, Q., Dong, Y.F., Feng, Y.P., and Ong, C.K. (2004) *Appl. Phys. Lett.*, **85**, 4418.

85 Rayner, G.B., Kang, D., Zhang, Y., and Lucovsky, G. (2002) *J. Vac. Sci. Technol. B*, **20**, 1748.

86 Sayan, S., Garfunkel, E., and Suzer, S. (2002) *Appl. Phys. Lett.*, **80**, 2135.

87 Afanas'ev, V.V., Stesmans, A., Chen, F., Shi, X., and Campbell, S.A. (2002) *Appl. Phys. Lett.*, **81**, 1053.

88 Sayan, S., Bartynski, R.A., Zhao, X., Gusev, E.P., Vanderbilt, D., Croft, M., Banaszak Holl, M., and Garfunkel, E. (2004) *Phys. Status Solidi B*, **241**, 2246.

89 Renault, O., Barrett, N.T., Samour, D., and Quiais-Marthon, S. (2004) *Surf. Sci.*, **566**, 526.

90 Bersch, E., Rangan, S., Bartynski, R.A., Garfunkel, E., and Vescovo, E. (2008) *Phys. Rev. B*, **78**, 085114.

91 Kralik, B., Chang, E.K., and Louie, S.G. (1998) *Phys. Rev. B*, **57**, 7027.

92 Fiorentini, V. and Gulleri, G. (2002) *Phys. Rev. Lett.*, **89**, 266101.

93 Dong, Y.F., Feng, Y.P., Wang, S.J., and Huan, A.C.H. (2005) *Phys. Rev. B*, **72**, 045327.

94 Tuttle, B.R., Tang, C., and Ramprasad, R. (2007) *Phys. Rev. B*, **75**, 235324.

95 Grüning, M., Shaltaf, R., and Rignanese, G.-M. (2010) *Phys. Rev. B*, **81**, 035330.

96 Shaltaf, R., Grüning, M., Stankovski, M., and Rignanese, G.-M., unpublished.

97 Morris, A.J., Stankovski, M., Delaney, K.T., Rinke, P., García-González, P., and Godby, R.W. (2007) *Phys. Rev. B*, **76**, 155106.

98 Tiago, M.L. and Chelikowsky, J.R. (2006) *Phys. Rev. B*, **73**, 205334.

99 Tiago, M.L., Idrobo, J.C., Öğüt, S., Jellinek, J., and Chelikowsky, J.R. (2009) *Phys. Rev. B*, **79**, 155419.

100 Van de Walle, C.G. and Neugebauer, J. (2004) *J. Appl. Phys.*, **95**, 3851.

101 Hedström, M., Schindlmayr, A., Schwarz, G., and Scheffler, M. (2006) *Phys. Rev. Lett.*, **97**, 226401.

102 Rinke, P., Janotti, A., Scheffler, M., and Van de Walle, C.G. (2009) *Phys. Rev. Lett.*, **102**, 026402.

103 Leung, W.-K., Needs, R.J., Rajagopal, G., Itoh, S., and Ihara, S. (1999) *Phys. Rev. Lett.*, **83**, 2351.

104 Batista, E.R., Heyd, J., Hennig, R.G., Uberuaga, B.P., Martin, R.L., Scuseria, G.E., Umrigar, J., and Wilkins, J.W. (2006) *Phys. Rev. B*, **74**, R121102.

105 Martin-Samos, L., Roma, G., Rinke, P., and Limoge, Y. (2010) *Phys. Rev. Lett.*, **104**, 075502.

106 Bruneval, F. (2009) *Phys. Rev. Lett.*, **103**, 176403.

107 Slater, J.C. (1974) *The Self-Consistent Field for Molecules and Solids*, vol. 4, McGraw-Hill, New York.